



## Synthesis of high performance Zr–Ca bifunctional catalysts and their catalytic ozonation effect for the decontamination of m-cresol wastewater

Lei Ma<sup>a</sup>, Yuan Zuo<sup>a</sup>, Jilong Xu<sup>a</sup>, Chunyu Tian<sup>a</sup>, Peiwei Han<sup>a</sup>, Huangzhao Wei<sup>b</sup>, Jianjun Gao<sup>c</sup>, Fentao Zhou<sup>c</sup>, Weijun Liu<sup>c,\*</sup>, Haibo Jin<sup>a,\*</sup>

<sup>a</sup>Beijing Key Laboratory of Fuels Cleaning and Advanced Catalytic Emission Reduction Technology/College of Chemical Engineering, Beijing Institute of Petrochemical Technology, Beijing 102617, China, Tel. +86-10-81292126; emails: jinhaibo@bipt.edu.cn (H. Jin), malei@bipt.edu.cn (L. Ma), 1336080320@qq.com (Y. Zuo), 1811911110@qq.com (J. Xu), 2221516610@qq.com (C. Tian), hanpeiwei025@126.com (P. Han)

<sup>b</sup>Dalian Institute of Chemical Physics, Chinese Academy of Sciences, Dalian 116023, China, Tel. +86-411-84379326; email: weihuangzhao@qq.com

<sup>c</sup>Shanxi Jinhuankeyuan Environmental Resources Technology Co., Ltd., Taiyuan, Shanxi 030024, China, Tel. +86-359-3965705; emails: liuweijun7041996@126.com (W. Liu), 51224375@qq.com (J. Gao), 453394961@qq.com (F. Zhou)

Received 27 August 2020; Accepted 28 December 2020

### ABSTRACT

This study proposes a new fabrication of fresh perovskite-based Zr–Ca catalysts. The catalytic behaviors of the bifunctional catalysts prepared by the co-precipitation method were examined during ozonation of m-cresol, a model organic pollutant. The catalysts outperformed the other tested catalysts in the catalytic ozonation of pollutants. The catalytic activity was favored by an aging temperature of 140°C and a calcination temperature in the 700°C–900°C range. The samples were characterized by X-ray diffraction, scanning electron microscopy, and high-resolution transmission electron microscopy. The most active catalysts were composed of two phases, CaZrO<sub>3</sub> and ZrO<sub>2</sub>. From X-ray photoelectron spectroscopy and in situ Fourier transform infrared studies, we inferred the nature of the active sites and a possible reaction mechanism. The mechanism was suggested as a non-radical mechanism.

*Keywords:* Catalytic ozonation; CaZrO<sub>3</sub>; ZrO<sub>2</sub>; Bifunctional catalysts; Clean water and sanitation

### 1. Introduction

Rapid industrial developments have proliferated the amounts of effluents from industrial plants. Unless properly treated or discharged, effluents such as coal conversion products, petrochemicals, and pharmaceuticals cause severe environmental contamination [1]. Despite intense efforts to improve eco-environments and develop technologies that remove toxic organics from aqueous solution, the continuing deterioration of water environments [2] demands much more attention. One of the most important

chemical products, m-cresol, is also a common wastewater pollutant. Listed as a priority pollutant by the United States Environmental Protection Agency, m-cresol has been adopted as a model pollutant in various research studies [3,4]. As m-cresol cannot be effectively removed by traditional approaches, it requires advanced oxidation processes (AOPs) with strongly oxidizing, non-selective, and environmental friendly characteristics [5,6].

One promising AOP is ozonation, which has efficiently degraded and mineralized recalcitrant pollutants [7,8]. Catalytic ozonation has been applied to effluents showing a certain refractory character toward non-catalytic ozonation.

\* Corresponding authors.

Catalytic ozonation research has focused on catalysts such as activated carbon, metal ions, metal oxides, and natural minerals [9,10], which play a key role in oxidizing pollutants. Heterogeneous catalysts more efficiently promote both conversion and mineralization of organics than homogeneous catalysts, and are readily separated from wastewater [11,12].

Perovskite-type oxides with the general formula  $ABO_3$  (where A is a rare or alkaline earth metal and B is a first-row transition metal) have dominated photocatalysis research [13,14]. Moreover, perovskite-type catalysts have been successfully utilized in catalytic wet peroxide oxidation and catalytic ozonation [15–18]. Such catalysts are stable at high temperatures and in aggressive media. The perovskite structure stabilizes the transition metal ions in rigorous oxidation states and enhances the oxygen mobility. Taran et al. [17] tested five perovskite oxides ( $LaCuO_3$ ,  $LaFeO_3$ ,  $LaMnO_3$ ,  $LaNiO_3$ ,  $LaCoO_3$ ) in the catalytic wet peroxide oxidation of phenol. The total organic carbon (TOC) depletion was 86% over  $LaCuO_3$ , 44% over  $LaFeO_3$ , and 0% over the others [17,19], demonstrating great variety in catalytic ability.

Calcium zirconate ( $CaZrO_3$ ) is an important perovskite-type material with many applications, such as luminescent materials [20,21], humidity sensors [22], ceramic capacitors [23], and protective materials at ultra-high temperatures [24,25]. However, in theoretical analyses of catalytic applications, this material has been much less studied than other perovskite oxides. Hence, investigating the catalytic ozonation potential of  $CaZrO_3$  in the degradation of biorefractory organics is a worthwhile task. In our preliminary experiments, a combined catalyst of  $CaZrO_3$  and  $ZrO_2$  delivered excellent catalytic ozonation performance. In this study, we synthesized and newly tested a series of Zr–Ca bifunctional catalysts for catalytic ozonation of m-cresol. Given the decisive impact of preparation methods on the textural properties and phase purity of perovskites, our main objective is to understand how the synthesis conditions (namely, the aging and calcination temperatures) affect the catalytic activity of m-cresol removal. From the structures, morphologies and components of the catalysts fabricated under various conditions, we illuminate the catalytic activity, mechanism, and stability in catalytic ozonation.

## 2. Experimental setup

### 2.1. Preparation of catalysts

Specified amounts of eight-hydrated zirconium chloride and anhydrous calcium chloride were weighed separately and transferred into 100 mL deionized water. Ammonium oxalate ( $1.9280 \pm 0.0005$  g), polyvinyl alcohol (molecular weight 20,000) and deionized water were added, along with ammonium hydroxide for pH regulation at 9.0–9.5. The solution was stirred at  $500 \pm 10$  rpm for 1 h by a magnetic stirring apparatus. The colloid was aged at various temperatures and then vacuum filtrated. The obtained sample was washed with deionized water, dried at  $120^\circ\text{C}$  for 12 h, and calcined at four different temperatures. Two batches of  $CaZrO_3$  perovskites were prepared for exploring the impacts of both aging and calcination

temperatures on the catalytic performance. For the first batch, the aging temperature was set at  $60^\circ\text{C}$ ,  $100^\circ\text{C}$ ,  $140^\circ\text{C}$ , or  $180^\circ\text{C}$ , and the calcination temperature was set to  $900^\circ\text{C}$ . These samples were named Zr–Ca-60, Zr–Ca-100, Zr–Ca-140, and Zr–Ca-180, respectively. The second batch was fabricated at constant aging temperature ( $140^\circ\text{C}$ ) and different calcination temperatures:  $700^\circ\text{C}$ ;  $800^\circ\text{C}$ ;  $900^\circ\text{C}$ ;  $1,000^\circ\text{C}$ ;  $1,100^\circ\text{C}$ ; or  $1,200^\circ\text{C}$ , forming samples Zr–Ca-700; Zr–Ca-800; Zr–Ca-900; Zr–Ca-1,000; Zr–Ca-1,100; and Zr–Ca-1,200, respectively.

### 2.2. Characterization of catalysts

X-ray diffraction (XRD) tests were performed on a German Bruker X-ray diffractometer (Bruker D8 Focus, Germany) with a CuK $\alpha$  radiation source. The wide-angle and small-angle scanning ranges were  $2\theta = 10^\circ\text{--}90^\circ$  and  $2\theta = 1^\circ\text{--}6^\circ$ , respectively. Scanning electron microscope (SEM) images of the catalyst were collected using a FEI Quanta 200 F instrument (province, country). The particle sizes of the active components were determined from transmission electron microscope (TEM) and high-resolution TEM (HRTEM) images of the catalyst collected at 100 kV by a HT7700 instrument (Hitachi Corporation, province, country). The elemental valence states of the catalysts were analyzed by X-ray photoelectron spectroscopy (ESCALAB 250Xi, Thermo Corporation, USA). The compositional changes during the reaction were detected as changes in the characteristic peaks of the elements detected by an attenuated total reflection sensor at the probe tip of a ReatIRTM15 instrument (Mettler Toledo, province, country), which monitored the changes in situ.

### 2.3. Reaction procedures and equipment

The catalytic ozonation reaction of m-cresol was carried out at room temperature as follows (Fig. 1 for the apparatus). In each run of experiments, 200 mL m-cresol (100 mg/L, no pH adjustment) and the catalyst (5 g/L) was placed in the reactor. The ozone concentration generated by the ozonator (CF-G-3-20g, Guolin Qingdao, China) was 50 mg/L (3.2 times the theoretical quantity), and the gas flow velocity was 160 mL/min. After 30 min of reaction, the samples were withdrawn from the aqueous phase and analyzed for TOC amount and m-cresol concentration. Additionally, the ozone concentrations in the gas phase of the inlet and outlet were measured by an Anseros Ozomat ozone analyzer (province, country). The ozonation efficiency was calculated as follows:

$$E = \frac{Q_i c_i - Q_0 c_0}{Q_i c_i} \times 100 \quad (1)$$

where  $Q_i$  and  $Q_0$  represent the volume flow rates of ozone at the reactor inlet and outlet, respectively, and  $c_i$  and  $c_0$  are the mass ozone concentrations at the reactor inlet and outlet, respectively.

## 3. Results and discussion

To investigate the m-cresol degradation performance of perovskite-based Zr–Ca composite in the catalytic

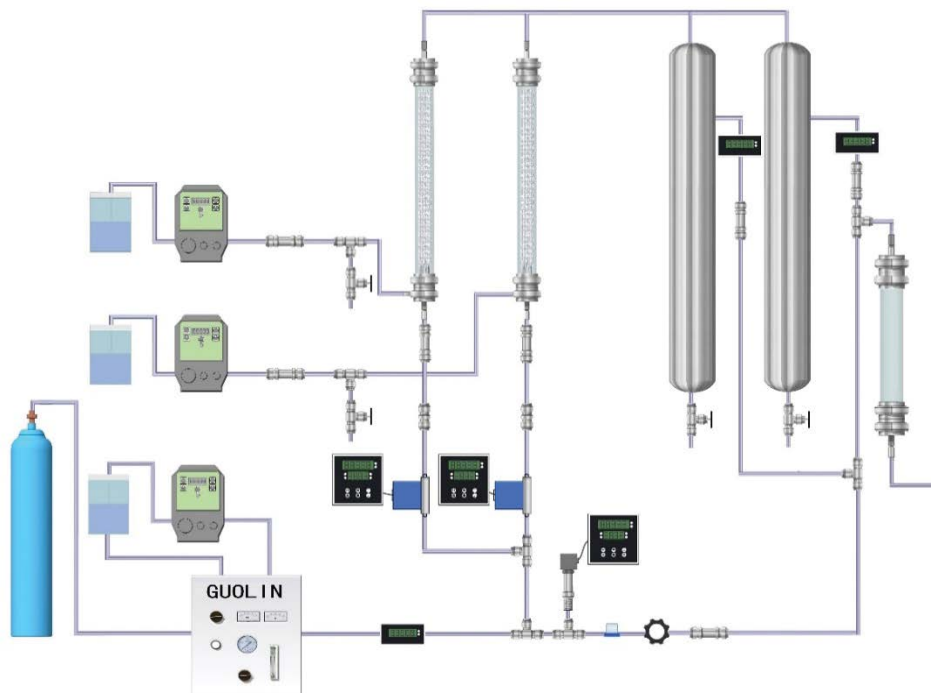


Fig. 1. Equipment of the catalytic ozonation analysis.

ozonation system, we compared the results of the catalysts made in our laboratory: ZSM-5, Fe/ZSM-5,  $\text{Al}_2\text{O}_3$ , 1% $\text{CeO}_2/\text{Al}_2\text{O}_3$ , 1% $\text{ZnO}/\text{Al}_2\text{O}_3$ , 1% $\text{NiO}/\text{Al}_2\text{O}_3$ , 0.5% $\text{Fe}_2\text{O}_3$ -0.5% $\text{MnO}_2/\text{Al}_2\text{O}_3$ , and 0.5% $\text{Fe}_2\text{O}_3$ -0.5% $\text{CuO}/\text{Al}_2\text{O}_3$  (Table 1). In the absence of catalyst, the TOC removal was extremely low (10.1%). In the catalytic systems, the TOC removal was more than doubled from that of the no-catalyst case. The highest and second-highest TOC removal rates were 61.4% (Zr-Ca-140) and 49.8% (1% $\text{CeO}_2/\text{Al}_2\text{O}_3$ ), respectively. Zr-Ca-14 also exhibited the highest  $\text{O}_3$  utilization. These results demonstrate the enormous potential of the newly synthesized  $\text{CaZrO}_3$ -based Zr–Ca bifunctional catalysts in treating organic effluents with a refractory nature. Therefore, we prepared a series of Zr–Ca bifunctional samples at different calcination and aging temperatures, and investigated the effects of these temperatures on the catalyst preparation.

The catalytic performances and characterizations were investigated on the 10 samples described in section 2.1. Both the aging and calcination temperatures significantly influenced the ingredients of the perovskite catalyst (Fig. 2). The XRD patterns of the catalysts aged at different temperatures exhibited a multiphase crystalline structure of  $\text{CaZrO}_3$  and  $\text{ZrO}_2$  [26] (Figs. 2a and b). The polymorphs of  $\text{CaZrO}_3$  and  $\text{ZrO}_2$  were orthorhombic and cubic, respectively. Most of the synthesized samples were composed of  $\text{CaZrO}_3$  and  $\text{ZrO}_2$ . In the XRD patterns of samples Zr-Ca-60 and Zr-Ca-180, the intensities of the  $\text{ZrO}_2$  and  $\text{CaZrO}_3$  peaks were higher and lower, respectively, than in the patterns of the other samples. Following the study by Gang and Sui [27], the molar ratios of  $\text{CaZrO}_3$  and  $\text{ZrO}_2$  were calculated as 1/2 (Zr-Ca-60) and 1/1.5 (Zr-Ca-180), respectively. Meanwhile, the relative intensities of the  $\text{ZrO}_2$  and  $\text{CaZrO}_3$  peaks in the XRD patterns of samples

Table 1

Capabilities of various catalysts in the catalytic ozonation of m-cresol

Catalyst	$X_{\text{TOC}}\%$	$\text{O}_3$ utilization mg TOC/g $\text{O}_3$
$\text{O}_3$ without catalyst	10.1	6.41
ZSM-5	23.4	15.10
Fe/ZSM-5	35	22.44
$\text{Al}_2\text{O}_3$	26.1	14.3
1% $\text{CeO}_2/\text{Al}_2\text{O}_3$	49.8	31.4
1% $\text{ZnO}/\text{Al}_2\text{O}_3$	44.3	25.6
1% $\text{NiO}/\text{Al}_2\text{O}_3$	43.6	28.3
0.5% $\text{Fe}_2\text{O}_3$ -0.5% $\text{MnO}_2/\text{Al}_2\text{O}_3$	43.9	27.4
0.5% $\text{Fe}_2\text{O}_3$ -0.5% $\text{CuO}/\text{Al}_2\text{O}_3$	47.5	28.4
Zr-Ca-140	61.4	30.7

Zr-Ca-100 and Zr-Ca-140 were reversed from those of Zr-Ca-60 and Zr-Ca-180. Accordingly, the molar ratios of  $\text{CaZrO}_3$  in Zr-Ca-100 and  $\text{ZrO}_2$  in Zr-Ca-140 were determined as 1/1.2 and 1/1, respectively. As shown in Fig. 2b, the TOC removal was higher on the Zr-Ca-100 (58%) and Zr-Ca-140 (61.4%) ozonation catalysts than on the Zr-Ca-60 (32%) and Zr-Ca-180 (45%) catalysts. Similarly, the highest  $\text{O}_3$  utilization was achieved by Zr-Ca-140 (39.28 mg TOC/g $\text{O}_3$ ). It seemed that the molar ratio of  $\text{CaZrO}_3$  and  $\text{ZrO}_2$  significantly influenced the catalytic ozonation capacity of the Zr–Ca bifunctional catalysts.

The XRD patterns of the catalysts calcined at different temperatures (700°C–1,000°C at 100°C intervals) also

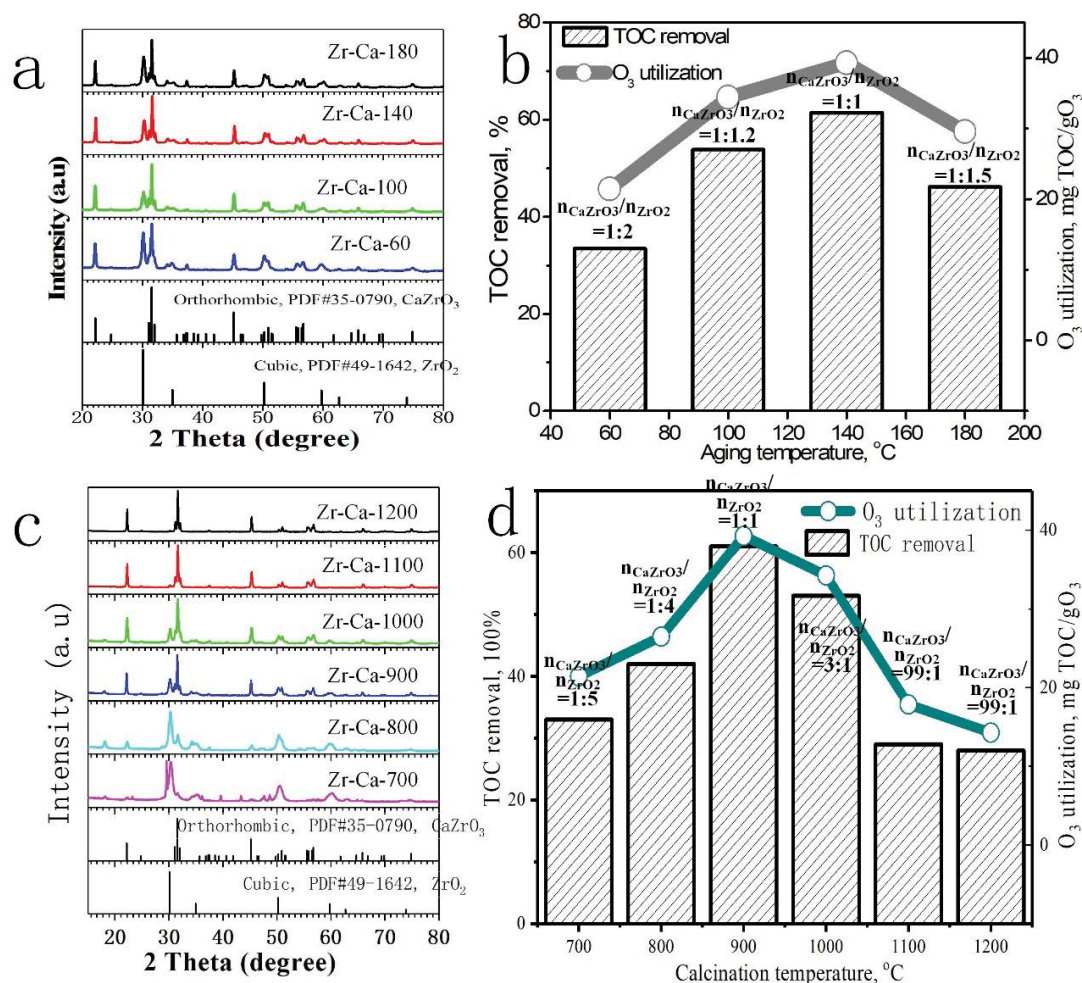


Fig. 2. X-ray diffraction patterns and TOC removal performances of the perovskite catalysts synthesized at different aging and calcination temperatures.

exhibited a multiphase crystalline structure of  $\text{CaZrO}_3$  and  $\text{ZrO}_2$  (Figs. 2c and d). At the low calcination temperatures ( $700^\circ\text{C}$  and  $800^\circ\text{C}$ ), the  $\text{ZrO}_2$  peak was extremely strong, while the  $\text{CaZrO}_3$  peak was insignificant. When calcined at these temperatures, the samples were dominated by  $\text{ZrO}_2$  and only a small amount of  $\text{CaZrO}_3$  was formed. When the calcination temperature increased to  $1,000^\circ\text{C}$ , the peak intensity of  $\text{CaZrO}_3$  was significantly enhanced while the peak intensity of  $\text{ZrO}_2$  declined. At higher calcination temperatures ( $1,100^\circ\text{C}$  and  $1,200^\circ\text{C}$ ), the XRD peaks of  $\text{ZrO}_2$  nearly disappeared, implying that when the samples were calcined at these temperatures, the  $\text{ZrO}_2$  was almost completely transformed to  $\text{CaZrO}_3$  [27]. As shown in Fig. 2, raising the calcination temperature from  $700^\circ\text{C}$  to  $900^\circ\text{C}$  improved the pollutant degradation performance, but at higher calcination temperatures (from  $900^\circ\text{C}$  to  $1,200^\circ\text{C}$ ), the performance decreased.

Relatively low calcination temperatures ( $700^\circ\text{C}$ – $900^\circ\text{C}$ ) favored the abatement of organics and the TOC removal reached around 40%. Conversely, raising the calcination temperature from  $900^\circ\text{C}$  to  $1,200^\circ\text{C}$  appreciably reduced the TOC removal from 58% to 28%. As also depicted in Fig. 2, the

ozonation utilization echoed the trend of TOC removal. The rather low TOC removal at calcination temperatures above  $1,000^\circ\text{C}$  was related to the uniform structure of the catalyst, in which the  $\text{ZrO}_2$  was synthesized almost as single-phase  $\text{CaZrO}_3$ .

Fig. 3 compares the catalytic ozonation performances of the Zr–Ca composite catalysts. As shown in panels (a) and (c), 100% of the m-cresol was converted during the ozonation process. When the catalysts were introduced to the reaction, 100% conversion was achieved after just 9 min of reaction, demonstrating the strong catalytic capacity of the Zr–Ca composite catalysts. The high catalytic capacity of Zr–Ca composite was reconfirmed in the TOC removal curves (Figs. 3b and d). On the Zr–Ca-140 (Zr–Ca-900) catalyst, the TOC removal was maximized to more than triple that of the TOC removal without catalyst (21%). From Figs. 2 and 3, it was inferred that both excessive zirconia and calcium zirconate were detrimental to catalyst activity, suggesting that  $\text{CaZrO}_3$  and  $\text{ZrO}_2$  play a synergistic role that boosts the pollutant degradation effect [28]. Fig. 4 compares the XRD patterns (Fig. 4a) and Brunauer–Emmett–Teller (BET) results (Figs. 4b and c) of

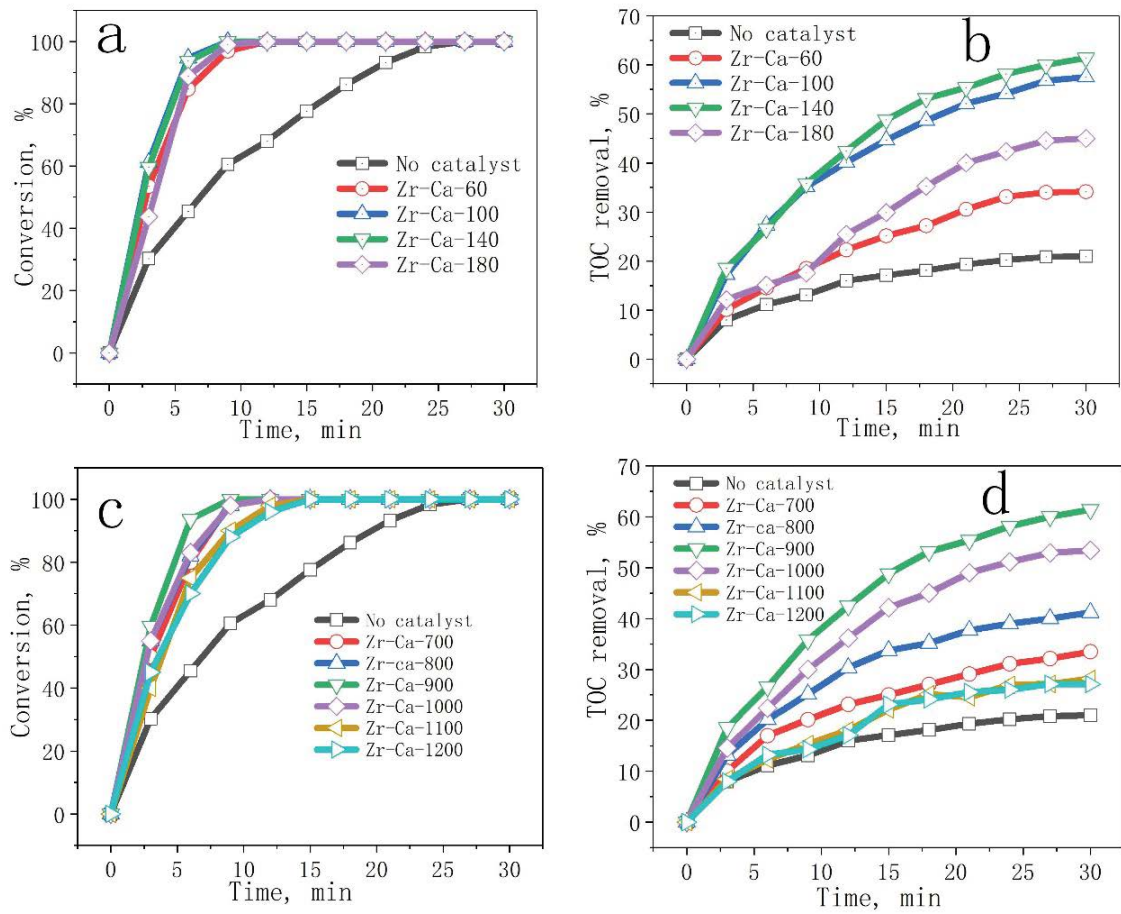


Fig. 3. Conversion (a), (c) and TOC removal (b), (d) of m-cresol on the Zr-Ca composites.

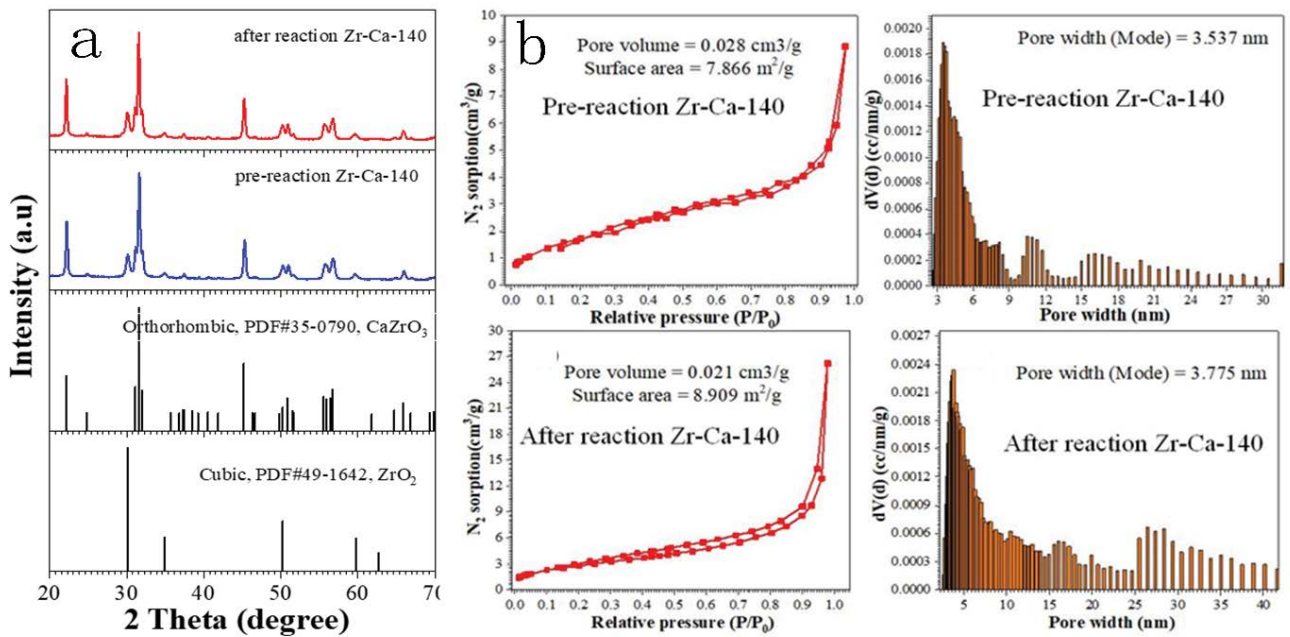


Fig. 4. XRD (a) and BET (b), (c) analyses of the unreacted and reacted Zr-Ca-140 catalyst.

the Zr-Ca-140 catalyst before and after the reaction. The small post-reaction changes indicate the excellent stability of the Zr-Ca-140 catalysts. The BET specific surface areas of the Zr-Ca catalyst were extremely low (no more than  $10 \text{ m}^2/\text{g}$ ; Fig. 4b), indicating that a very small amount of the pollutant was removed by adsorption to the Zr-Ca composites.

Fig. 5 displays the SEM and HRTEM images of catalysts fabricated at the four aging temperatures. The surface topography of the sample aged at  $140^\circ\text{C}$  exhibited a more normally distributed crystallite size and better developed porosity than the other samples. As seen in the particle size distributions (top row of Fig. 5, insets), lowering the aging temperature reduced the size of the formed particles. The average particle size of the catalyst aged at  $140^\circ\text{C}$  ( $2.55 \mu\text{m}$ ) was larger than those of the catalysts aged at  $60^\circ\text{C}$  and  $100^\circ\text{C}$  ( $1.77$  and  $2.07 \mu\text{m}$ , respectively), but smaller than that of the catalyst aged at  $180^\circ\text{C}$ . From the HRTEM images (bottom row of Fig. 5) and pore size distributions (Fig. 4c), the four  $\text{ZrO}_2$ - $\text{CaZrO}_3$  composite samples were inferred to be assembled as typical nanosheets smaller than  $10 \text{ nm}$  in width [29]. The HRTEM images also demonstrated a  $\text{ZrO}_2$  and  $\text{CaZrO}_3$  composition of the samples, consistent with the XRD patterns in Fig. 2.

Fig. 6 shows the XPS spectra of Ca and Zr in the composite catalysts aged at different temperatures. Typical asymmetrical peaks appeared in the Zr  $3d$  and Ca  $2p$  regions (Fig. 6a and b). The peaks located at  $183.4$ – $183.5 \text{ eV}$  and  $180.9$ – $181.5 \text{ eV}$  were associated with Zr  $3d_{3/2}$  and Zr  $3d_{5/2}$ , respectively, indicating the presence of  $\text{Zr}^{4+}$  [27]. Meanwhile, the peaks at  $349.6$ – $350.3$  and  $346.2$ – $346.7 \text{ eV}$  were assigned to  $\text{Ca}2p_{1/2}$  and  $\text{Ca}2p_{3/2}$ , respectively, possibly indicating Ca-OH. Such Ca-OH bonds might appear at the adsorption sites of m-cresol. As the aging temperature rose from  $100^\circ\text{C}$  to  $180^\circ\text{C}$ , the binding energies

of the Zr  $3d_{3/2}$  and Zr  $3d_{5/2}$  peaks shifted leftward, implying that electrons were transferred from Ca to Zr and then to oxidizing agents (e.g.,  $\text{O}_3$ ) at the catalyst surface [27,29]. Water adsorbed on the  $\text{CaZrO}_3$  surface induced hydrolytic dissociation to Ca-OH, aided by the  $\text{O}_3$  adsorbed on the  $\text{ZrO}_2$  surface.

To investigate the O variation in the surface chemistry as the aging temperature increased, the O  $1s$  spectra were deconvoluted into two peaks (Fig. 6c). The peaks centered at  $529.4$ – $529.7 \text{ eV}$  (termed the  $\text{O}_L$  peaks) and  $531$ – $531.5 \text{ eV}$  (termed the  $\text{O}_S$  peaks) represented surface lattice oxygen and surface adsorbed oxygen, respectively [30]. As shown in Fig. 6c, the proportion of the  $\text{O}_S$  peak was lowest in the XPS O  $1s$  spectra of Zr-Ca-140 ( $63.19\%$ ), suggesting that on this catalyst, more surface active sites were available for adsorption of the  $\text{O}_3$  bubbled into the system than on the other catalysts. The proportions of  $\text{O}_S$  in the Zr-Ca-180 and Zr-Ca-60 catalysts were  $67.31\%$  and  $68.75\%$ , respectively. It was inferred that the usual active sites of the catalyst were  $\text{O}_L$  [31] and that surface-adsorbed oxygen ( $\text{O}_S$ ) restricted the adsorption of  $\text{O}_3$ . Electron paramagnetic resonance (Fig. 7), detected no hydroxyl radicals in the ozonation of m-cresol with the Zr-Ca-140 catalyst. This result clarifies the high performance of Zr-Ca-140 in the ozonation of m-cresol.

Zhang et al. [32] proposed a non-radical ozonation mechanism in the catalytic ozonation system. They considered that  $\text{O}_3$  adsorbs on the PdO sites of the catalyst, where it decomposes into surface atomic oxygen ( $^*\text{O}$ ) [32]. They attributed the high activity of the catalyst to the synergistic function of bi-component catalysts. Fig. 1 implies that the high catalytic performance of the Zr-Ca-140 and Zr-Ca-100 samples was also conferred by a synergistic function of their bi-components ( $\text{ZrO}_2$  and  $\text{CaZrO}_3$ ). The

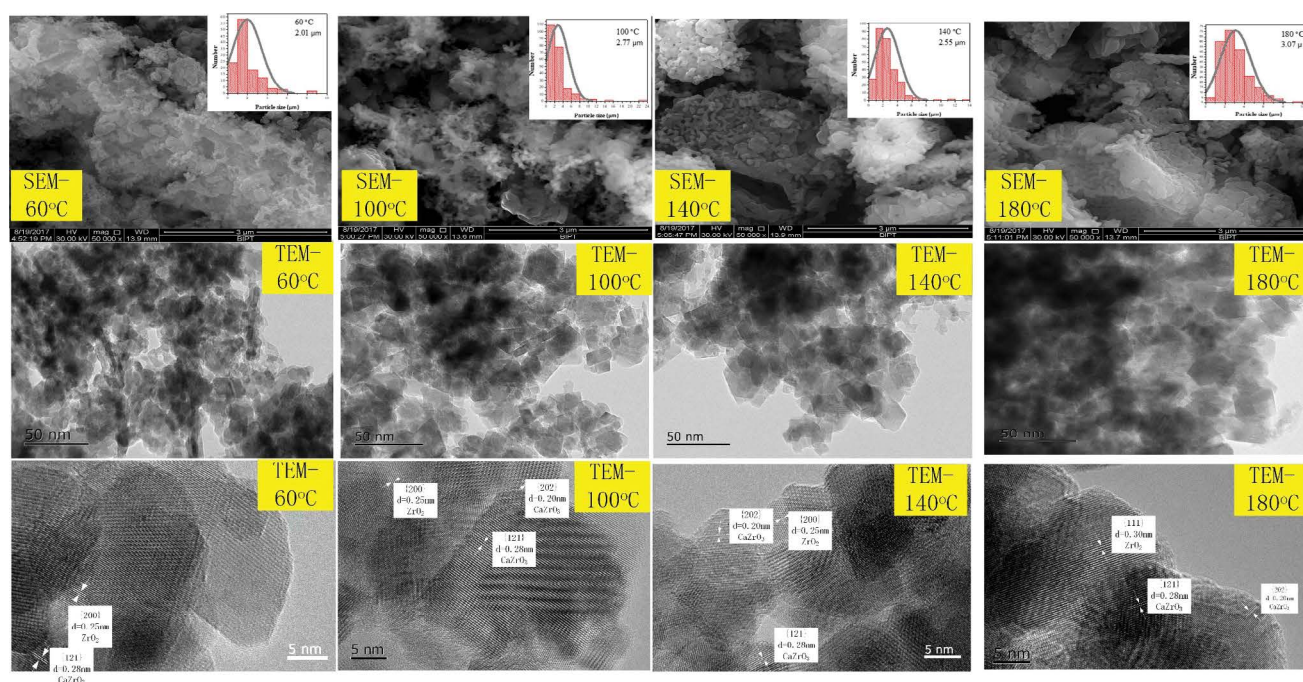


Fig. 5. Scanning electron microscope and TEM images of the perovskite catalysts synthesized at different aging temperatures.

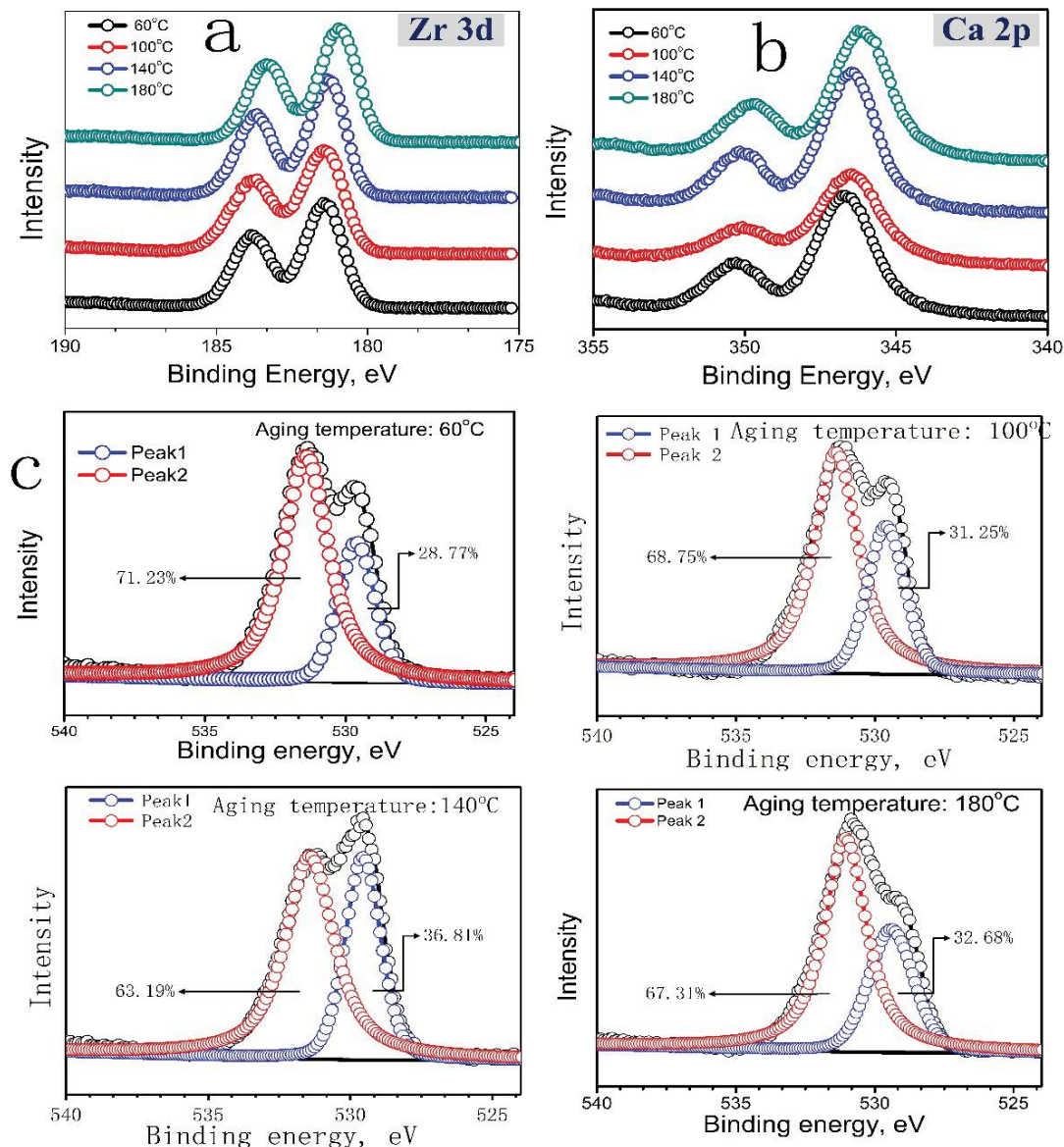
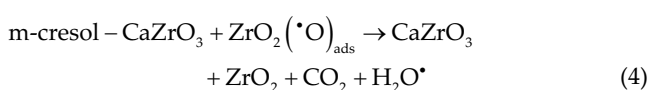
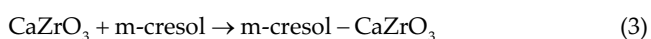
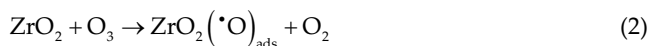


Fig. 6. XPS spectra of Zr 3d (a), Ca 2p (b) and O1s (c) of the Zr–Ca composite catalysts aged at different temperatures.

catalytic ozonation mechanism in this paper can thus be summarized as follows (Fig. 8):



First,  $\text{O}_3$  adsorbs to the surface active  $\text{O}_L$  sites of  $\text{ZrO}_2$ , where it decomposes into atomic O ( $\cdot\text{O}$ ) (Eq. (2)). Aided by the Ca–OH bonds, the pollutant (m-cresol) adsorbs to the

surface of  $\text{CaZrO}_3$  (Eq. (3)). Finally, the O atoms adsorbed on  $\text{ZrO}_2$  oxidize the m-cresol adsorbed on  $\text{CaZrO}_3$  into  $\text{CO}_2$  and  $\text{H}_2\text{O}$  (Eq. (4)).

To obtain further insights into the aforementioned TOC removal, the intermediate products during the catalytic oxidation were scrutinized by monitoring the situ degradation of m-cresol with an in situ IR monitoring system (React IR). The React IR results are shown in Fig. 9. The instrument captured the characteristic peaks of m-cresol centered at 1,156; 1,279; 1,491; and 1,592  $\text{cm}^{-1}$ . The peaks at 1,156 and 1,279  $\text{cm}^{-1}$  were associated with stretching vibrations of C–O and C=C, respectively. The peaks centered at 1,491 and 1,592  $\text{cm}^{-1}$  represent the deformation vibrations inside and outside of the benzene ring [33,34]. As the reaction proceeded, the intensity of the featured peaks weakened rapidly, indicating fast degradation of

m-cresol in the reaction system. In contrast, the absorption peaks located at 1,592; 2,170; and 2,206  $\text{cm}^{-1}$  initially decreased and then intensified as the reaction proceeded. This behavior probably reflects the formation of intermediate products during the degradation of m-cresol. When the peaks representing m-cresol diminished, the absorption peaks of the newly generated substances strengthened correspondingly. As the 1,592 and 2,206  $\text{cm}^{-1}$  characterize C=C and  $-\text{COO}-$ , respectively, the probable intermediate substances were unsaturated carboxylic acids.

The above analysis clarified the degradation mechanism of m-cresol on the Zr–Ca composites. Furthermore, the stability of the Zr–Ca catalysts was explored through continuous reaction experiments (Fig. 10). A columnar Zr–Ca-140 catalyst obtained by the tableting method (Fig. 10a) was applied to the continuous degradation reaction of m-cresol by catalyzed ozonation. The reaction results are shown in Fig. 10b. With or without the catalyst, the ozonation reaction converted 100% of the m-cresol within 100 h. However, the TOC removal by ozonation largely depended on the catalyst. Without the catalyst, the m-cresol ozonation removed only approximately 50% of the TOC, whereas the catalyst improved the TOC removal to 80%. These

findings clarify the strong stability and high activity of Zr–Ca-140 catalyst in the catalytic ozonation reaction.

#### 4. Conclusion

Bi-component catalysts were synthesized by the coprecipitation method and tested on the ozonation oxidation of m-cresol. The catalysts exhibited excellent catalytic ozonation capacity. The TOC removal ability and  $\text{O}_3$  utilization differed among the catalysts prepared at different aging temperatures ( $60^\circ\text{C}$ – $180^\circ\text{C}$ ) and calcination temperatures ( $700^\circ\text{C}$ – $1,200^\circ\text{C}$ ). The aging and calcination temperatures markedly affected the structures of the catalysts. Interestingly, the pure  $\text{CaZrO}_3$  or  $\text{ZrO}_2$  phase did not achieve the best organic degradation. Combining the XRD, HRTEM and TOC removal results, we concluded that the composite material with equal molar proportions of  $\text{CaZrO}_3$  and  $\text{ZrO}_2$  was the most active (TOC removal = 61.4%). The in situ FTIR spectra indicated that while m-cresol was reduced during the reaction, new unsaturated carboxylic acids were formed. From a comparative XPS study of Zr, Ca and O in the catalysts aged at different temperatures, a non-radical ozonation mechanism was inferred. Hence, the heterogeneous-phase  $\text{CaZrO}_3$ -based perovskite is a promising catalyst for the oxidation of organic substrates with ozone in aqueous solutions.

#### Acknowledgments

This research was funded by Project of Construction of Innovative Teams and Teacher Career Development for Universities and Colleges under Beijing Municipality (IDHT20180508), Scientific Research Common Program of Beijing Municipal Commission of Education (KM202010017006), Shipei Project of Beijing Municipal Commission of Education, the Talents Project of Beijing Organization Department (2018000020124G091), the Strategic Priority Research Program of the Chinese Academy of Sciences (XDA21021101) and the National Key Research and Development Program of China (Grant NO. 2019YFA0705803).

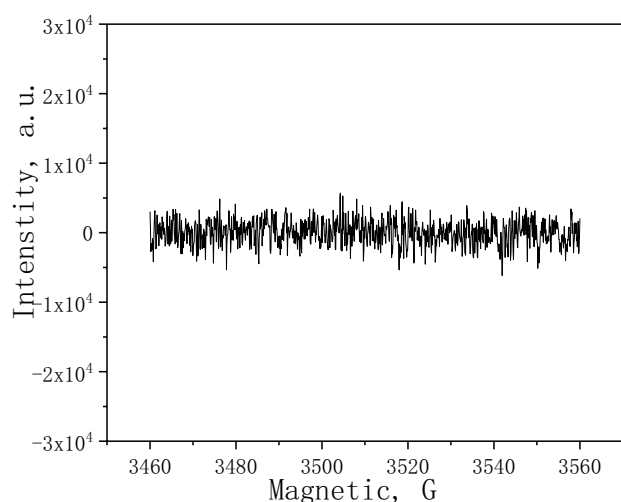


Fig. 7. EPR test of ozonation with Zr–Ca-140 as catalyst.

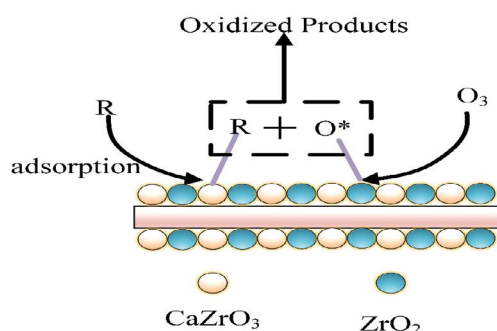


Fig. 8. Proposed catalytic mechanism of Zr–Ca catalysts in the ozonation of m-cresol.

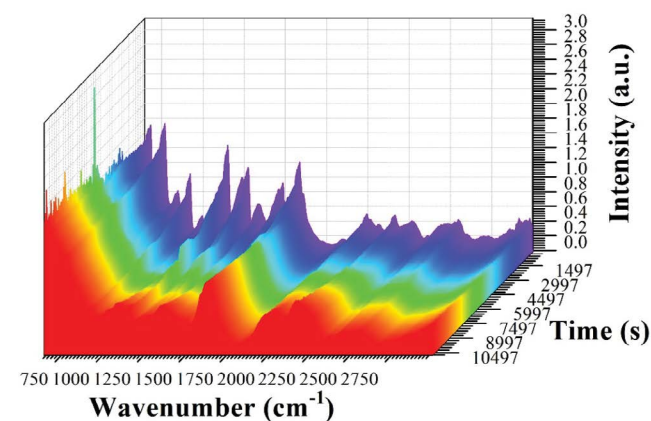


Fig. 9. In situ infrared reaction data of catalytic ozonation of m-cresol on the perovskite catalysts.

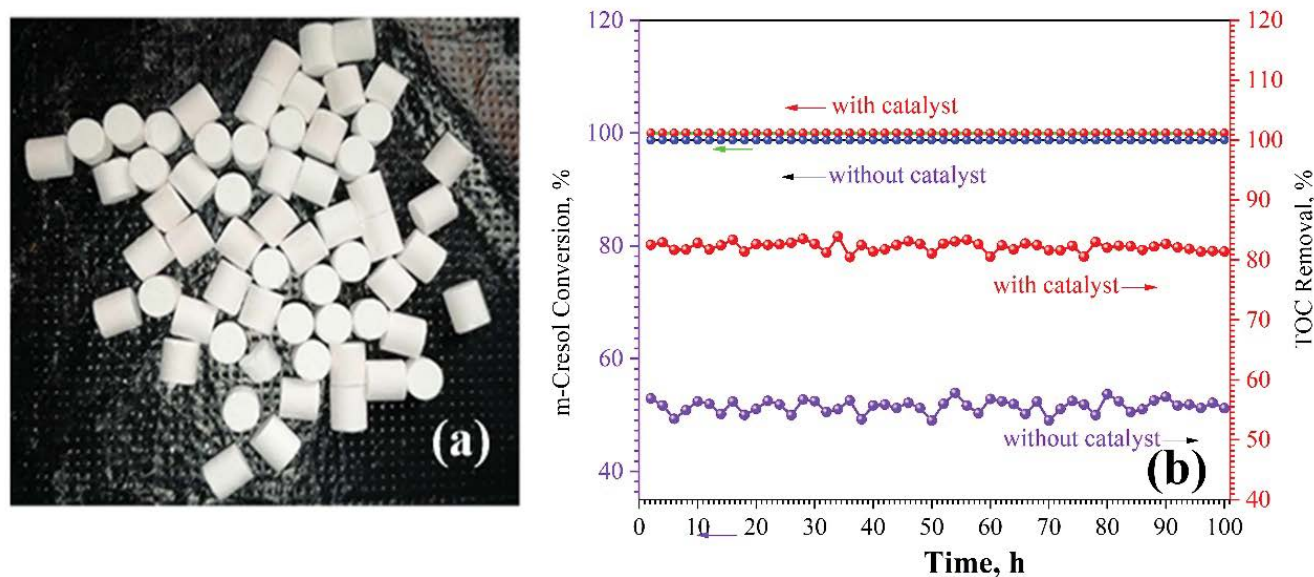


Fig. 10. (a) Appearance of the Zr-Ca-140 catalyst and (b) comparison of the continuous reaction results with and without Zr-Ca-140.

## References

- [1] L. Ma, Z. Chen, C. Xu, F. Li, H. Jin, L. Shi, H.-Y. Hu, Water Meta-cycle model and indicators for industrial processes- the pulp & paper case in China, *Resour. Conserv. Recycl.*, 139 (2018) 228–236.
- [2] W. Duan, F. Meng, H. Cui, Y. Lin, G. Wang, J. Wu, Ecotoxicity of phenol and cresols to aquatic organisms: a review, *Ecotoxicol. Environ. Saf.*, 157 (2018) 441–456.
- [3] Y. Wang, H. Wei, Y. Zhao, W. Sun, C. Sun, The optimization, kinetics and mechanism of m-cresol degradation via catalytic wet peroxide oxidation with sludge-derived carbon catalyst, *J. Hazard. Mater.*, 326 (2017) 36–46.
- [4] L. Ma, C. Jin, L. An, L. Huang, L. Li, H. Jin, B. Liang, H. Wei, C. Sun, Preliminary investigation of the degradation mechanism of o, m and p-cresol using sludge-derived carbon nanosheets by catalytic oxidation based on quantum chemistry, *Catal. Commun.*, 120 (2019) 59–65.
- [5] L. Ma, C. Sun, J. Ren, H. Wei, P. Liu, Efficient electrochemical incineration of phenol on activated carbon fiber as a new type of particulates, *Russ. J. Electrochem.*, 50 (2014) 569–578.
- [6] L. Ma, B. Yu, Y.H. Yu, J.M. Li, J. Ren, H.Z. Wei, C.L. Sun, Indirect electrochemical oxidation of pentachlorophenol in the presence of different halides: behavior and mechanism, *Desal. Water Treat.*, 52 (2014) 1462–1471.
- [7] H. Zhuang, H. Han, B. Hou, S. Jia, Q. Zhao, Heterogeneous catalytic ozonation of biologically pretreated Lurgi coal gasification wastewater using sewage sludge based activated carbon supported manganese and ferric oxides as catalysts, *Bioresour. Technol.*, 166 (2014) 178–186.
- [8] L. Yu, P. Han, H. Jin, H. Wei, W. Liu, L. Ma, C. Xu, Catalytic ozonation of three isomeric cresols in the presence of NaCl with nano-mesoporous  $\beta$ -molecular sieves, *Process Saf. Environ.*, 129 (2019) 63–73.
- [9] F. Zhang, K. Wu, H. Zhou, Y. Hu, P. Sergei, H. Wu, C. Wei, Ozonation of aqueous phenol catalyzed by biochar produced from sludge obtained in the treatment of coking wastewater, *J. Environ. Manage.*, 224 (2018) 376–386.
- [10] J. Nawrocki, B. Kasprzyk-Hordern, The efficiency and mechanisms of catalytic ozonation, *Appl. Catal. B*, 99 (2010) 27–42.
- [11] S. Zhang, X. Quan, D. Wang, Catalytic ozonation in arrayed zinc oxide nanotubes as highly efficient mini-column catalyst reactors (MCRs) augmentation of hydroxyl radical exposure, *Environ. Sci. Technol.*, 52 (2018) 8701–8711.
- [12] M. Kermani, B. Kakavandi, M. Farzadkia, A. Esrafil, S.F. Jokandan, A. Shahsavani, Catalytic ozonation of high concentrations of catechol over  $\text{TiO}_2/\text{Fe}_3\text{O}_4$  magnetic core-shell nanocatalyst: optimization, toxicity and degradation pathway studies, *J. Cleaner Prod.*, 192 (2018) 597–607.
- [13] E. Grabowska, Selected perovskite oxides: characterization, preparation and photocatalytic properties—a review, *Appl. Catal. B*, 186 (2016) 97–126.
- [14] P. Wu, J. Shi, Z. Zhou, W. Tang, L. Guo,  $\text{CaTaO}_2\text{N}-\text{CaZrO}_3$  solid solution: Band-structure engineering and visible-light-driven photocatalytic hydrogen production, *Int. J. Hydrogen Energy*, 37 (2012) 13704–13710.
- [15] R.C. Martins, R.M. Quinta-Ferreira, Catalytic ozonation of phenolic acids over a Mn–Ce–O catalyst, *Appl. Catal. B*, 90 (2009) 268–277.
- [16] M. Carbajo, F.J. Beltrán, O. Gimeno, B. Acedo, F.J. Rivas, Ozonation of phenolic wastewaters in the presence of a perovskite type catalyst, *Appl. Catal. B*, 74 (2007) 203–210.
- [17] O.P. Taran, A.B. Ayusheev, O.L. Ogorodnikova, I.P. Prosvirin, L.A. Isupova, V.N. Parmon, Perovskite-like catalysts  $\text{LaBO}_3$  (B = Cu, Fe, Mn, Co, Ni) for wet peroxide oxidation of phenol, *Appl. Catal. B*, 180 (2016) 86–93.
- [18] S. Afzal, X. Quan, J. Zhang, High surface area mesoporous nanocast  $\text{LaMO}_3$  (M = Mn, Fe) perovskites for efficient catalytic ozonation and an insight into probable catalytic mechanism, *Appl. Catal. B*, 206 (2017) 692–703.
- [19] Y. Zhang, Q. Li, Y. Long, J. Zou, Z. Song, C. Liu, L. Liu, F. Qi, B. Xu, Z. Chen, Catalytic ozonation benefit from the enhancement of electron transfer by the coupling of  $\text{g-C}_3\text{N}_4$  and  $\text{LaCoO}_3$ : discussion on catalyst fabrication and electron transfer pathway, *Appl. Catal. B*, 254 (2019) 569–579.
- [20] B. Evangelina, P.A. Azeem, R. Prasada Rao, G. Swati, D. Haranath, Structural and luminescent features of cerium doped  $\text{CaZrO}_3$  blue nanophosphors, *J. Alloys Comp.*, 705 (2017) 618–623.
- [21] Y.M. Ji, D.Y. Jiang, Z.H. Wu, T. Feng, J.L. Shi, Combustion synthesis and photoluminescence of  $\text{Ce}^{3+}$ -activated  $\text{MHfO}_3$  (M = Ba, Sr, or Ca), *Mater. Res. Bull.*, 40 (2005) 1521–1526.
- [22] R.S. André, S.M. Zanetti, J.A. Varela, E. Longo, Synthesis by a chemical method and characterization of  $\text{CaZrO}_3$  powders: potential application as humidity sensors, *Ceram. Int.*, 40 (2014) 16627–16634.
- [23] G. Villalba, R.U. Ayres, H. Schroder, Accounting for fluorine: production, use, and loss, *J. Ind. Ecol.*, 11 (2007) 85–101.

- [24] D.P. Rai, Sandeep, A. Shankar, A.P. Sakhya, T.P. Sinha, B. Merabet, M. Musa Saad, H.-E.R. Khenata, A. Bouchani, S. Solaymani, R.K. Thapa, Electronic and optical properties of cubic SrHfO<sub>3</sub> at different pressures: a first principles study, *Mater. Chem. Phys.*, 186 (2017) 620–626.
- [25] F.J. Beltrán, J. Encinar, J.F. González, Industrial wastewater advanced oxidation. Part 2. Ozone combined with hydrogen peroxide or UV radiation, *Water Res.*, 31 (1997) 2420–2428.
- [26] C. Zhao, Z. Zhou, Z. Cheng, X. Fang, Sol-gel-derived, CaZrO<sub>3</sub>-stabilized Ni/CaO-CaZrO<sub>3</sub> bifunctional catalyst for sorption-enhanced steam methane reforming, *Appl. Catal. B*, 196 (2016) 16–26.
- [27] C. Gang, Q. Sui, An external standard method of quantitative phase analysis of the sample containing and amorphous phase by X-ray diffraction, *Acta. Metall. Sin.-Engl.*, 7 (1994) 179–182 (in Chinese).
- [28] Z. Kesic, I. Lukic, M. Zdujic, C. Jovalekic, V. Veljkovic, D. Skala, Assessment of CaTiO<sub>3</sub>, CaMnO<sub>3</sub>, CaZrO<sub>3</sub> and Ca<sub>2</sub>Fe<sub>2</sub>O<sub>5</sub> perovskites as heterogeneous base catalysts for biodiesel synthesis, *Fuel Process. Technol.*, 143 (2016) 162–168.
- [29] R. Koirala, K.R. Gunugunuri, S.E. Pratsinis, P.G. Smirniotis, Effect of zirconia doping on the structure and stability of CaO-based sorbents for CO<sub>2</sub> capture during extended operating cycles, *J. Phys. Chem. C*, 115 (2011) 24804–24812.
- [30] Y. Joseph, W. Ranke, W. Weiss, Water on FeO(111) and Fe<sub>3</sub>O<sub>4</sub>(111): adsorption behavior on different surface terminations, *J. Phys. Chem. C*, 104 (2000) 3224–3236.
- [31] C. Weerakkody, S. Biswas, W. Song, J. He, N. Wasalathanthri, S. Dissanayake, D.A. Kriz, B. Dutta, S.L. Suib, Controllable synthesis of mesoporous cobalt oxide for peroxide free catalytic epoxidation of alkenes under aerobic conditions, *Appl. Catal. B*, 221 (2018) 681–690.
- [32] T. Zhang, W. Li, J.P. Croué, Catalytic ozonation of oxalate with a cerium supported palladium oxide: an efficient degradation not relying on hydroxyl radical oxidation, *Environ. Sci. Technol.*, 45 (2011) 9339–9346.
- [33] S.J. Hug, D. Bahnemann, Infrared spectra of oxalate, malonate and succinate adsorbed on the aqueous surface of rutile, anatase and lepidocrocite measured with in situ ATR-FTIR, *J. Electron. Spectrosc. Relat. Phenom.*, 150 (2006) 208–219.
- [34] J. Zhuang, Q. Tian, S. Lin, W. Yang, L. Chen, P. Liu, Precursor morphology-controlled formation of perovskites CaTiO<sub>3</sub> and their photo-activity for As(III) removal, *Appl. Catal. B*, 156–157 (2014) 108–115.